Low-Level Wind Field Climatology over the La Plata River Region Obtained with a Mesoscale Atmospheric Boundary Layer Model Forced with Local Weather Observations

GUILLERMO J. BERRI*,+ AND LAURA SRAIBMAN

Department of Atmospheric and Oceanic Sciences, University of Buenos Aires, Buenos Aires, Argentina

RAUL A. TANCO

Faculty of Astronomical and Geophysical Sciences, University of La Plata, La Plata, Argentina

GERMAN BERTOSSA

National Meteorological Service, Buenos Aires, Argentina

(Manuscript received 12 August 2009, in final form 18 January 2010)

ABSTRACT

A primitive equation, dry, hydrostatic, and incompressible mesoscale boundary layer model is used to simulate the high-horizontal-resolution low-level wind field "climatology" over the La Plata River region in South America. The horizontal model domain has 79 × 58 points (350 km × 316 km), with a horizontal resolution of 0.05°. The model climatological field is the ensemble result of a series of daily forecasts obtained by forcing the model with limited local observations. Each ensemble member produces a daily forecast that participates in the definition of the wind climatology with a probability calculated with the local observations. The upper boundary condition is taken from the only local radiosonde observation, and the lower boundary condition consists of a surface heating function calculated with the temperature observations of the surface weather stations in the region. The study, conducted during the period of 1959–84, reveals an overall good agreement between the observed and the modeled surface wind climatological fields at five weather stations in the region. The model represents very well the differences in the wind speed magnitudes and predominant wind direction sectors throughout a region that displays a strong sea–land-breeze daily cycle. The average root-mean-square value of the model relative error is 31% for wind direction and 23% for wind speed. Model errors vary throughout the day with the minimum in the morning and afternoon and the maximum at night. The seasonal climatology shows the minimum wind direction error in winter and the maximum error in summer, whereas the wind speed errors reveal no seasonality. The annual wind direction error is very similar to the winter minimum error. The conclusion of the study is that the proposed ensemble mean method is useful for synthesizing high-resolution climatological low-level wind fields over regions with a strong diurnal cycle of surface thermal contrasts and a limited number of available weather stations.

1. Introduction

The region of the La Plata River in southeastern South America (see Fig. 1) concentrates important economic and social activities since one-third of the population of Argentina and more than one-half of the population of Uruguay live there. Large urban complexes, different commercial activities, and important industries are located along its shores. In addition, the La Plata River and its tributary the Paraná River are main ship tracks with some of the largest ports of the southern cone of South America. Therefore, the region is of vital importance for the two countries. The La Plata River is a large water surface that projects into the continent, conditioning the local weather and climate. Thus, other related environmental aspects are strongly influenced by the local weather and climate conditions, such as environmental

* Current affiliation: National Meteorological Service, Buenos Aires, Argentina.

+ Member of the National Research Council of Argentina (CONICET).

Corresponding author address: Guillermo J. Berri, Servicio Meteorológico Nacional, 25 de Mayo 658, C1002ABN Buenos Aires, Argentina.
E-mail: gberri@smn.gov.ar

DOI: 10.1175/2010JAMC2370.1

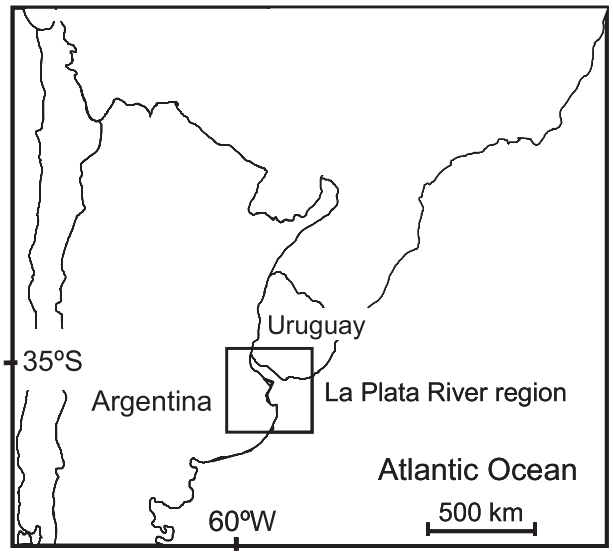

FIG. 1. Location of La Plata River region in South America.

pollution, water currents and tidal regime (Simionato et al. 2005), commercial fishing at the oceanic front, port operations, navigation, and tourism.

The La Plata River is 300 km long, with a variable width that is between 40 and 200 km. The region creates a considerable surface temperature contrast with the continent that sets the stage for the development of a low-level circulation, with sea–land-breeze characteristics. During the daytime hours the lower layers over land are warmer than over the river, creating a land–river surface temperature gradient that establishes a river-to-land wind component known as a sea breeze. Over the northern shore of the La Plata River the surface winds increase the southerly component while over the southern shore they increase the northerly wind component. The daytime inland surface wind components create horizontal divergence and subsidence over the river and convergence and upward motion over land near the river shores. During the nighttime hours the land is cooler than the river, the land–river surface temperature gradient reverses and the winds tend to blow from land to river, establishing the land breeze. The nighttime land breeze is not as well developed as the daytime sea breeze basically because of weaker low-level winds due to the nocturnal stability. The daily cycle of the land–river surface temperature contrast gives rise to significant changes in the predominant wind direction across the region throughout the day. This can be appreciated in Fig. 2, which shows the observed 1959–84 mean winds at five weather stations in the region. The weather stations used in the study are Ezeiza (EZE), Aeroparque (AER), Martín García (MGA), Punta Indio (PIN), and Pontón Recalada (PRE). At 0900 local standard time (LST) (Fig. 2a), all of the weather stations show predominant N and NE wind sectors that together amount to 30%–40% of the time. At 1500 LST (Fig. 2b), the weather stations over land in Argentina display the N, NE, and E wind sectors as the dominant ones, totaling 40%–60% of the time (in particular, AER has an E wind frequency of 23%). In contrast, the weather stations over the river display as dominant sectors the E, SE, and S wind directions. At 2100 LST (Fig. 2c), the dominant wind sector over land is E, followed by SE, as well as over PRE at the river mouth, whereas over MGA it is SE followed by E. The wind direction frequency distribution at 0300 LST (Fig. 2d) looks similar to that of 0900 LST. Table 1 shows the mean wind speed by wind sector at the four different times of the day. Throughout the day, the weather stations over the river display a significant change in the dominant wind sectors of more than one quadrant (90°–130°), while for the stations over land the daily change is less than one quadrant.

Atmospheric mesoscale models have the capability of reproducing the major aspects of the sea–land-breeze circulation when the horizontal thermal contrast is properly defined. Different numerical models have been employed for the study of this type of local circulations. For example, Pielke et al. (1992) describe the use of the Regional Atmospheric Modeling System (RAMS) in sea–land-breeze studies, employing telescopic and nested grids; Case et al. (2004) use RAMS coupled to the Eta Model to simulate the sea breeze over the eastern coast of the Florida peninsula; and Colby (2004) employs the fifth-generation Pennsylvania State University–National Center for Atmospheric Research Mesoscale Model (MM5) with different resolutions to study of the sea breeze over the New England coast.

Berri and Nuñez (1993) show that the sea–land-breeze circulation over the La Plata River region can be simulated with a mesoscale boundary layer model (BLM) that was specially developed for the region. The results obtained by the authors in a case study show good agreement between observed and modeled surface wind direction changes throughout the day. The daily cycle of the sea–land breeze responds to the atmospheric pressure anomaly field induced by the cyclic thermal contrast at the surface. Thus, the driving mechanism of the above-mentioned model is the daily variation of the horizontal temperature difference across the river shores. A recent study (Sraibman and Berri 2009) finds that operational low-level wind forecasts for the La Plata River region can be improved by running the BLM forced by the Eta Model operational forecasts. This study concludes that the improvement obtained with the BLM is a consequence of the appropriate definition of the land–river surface temperature contrast that is fundamental

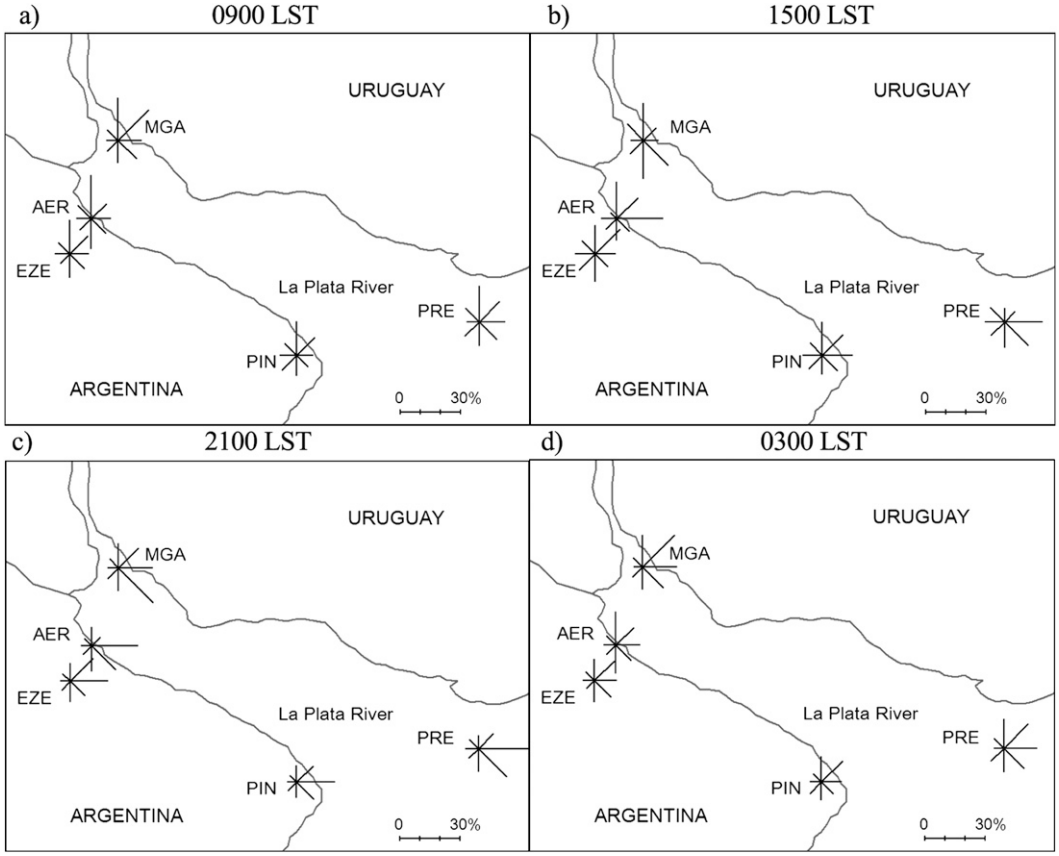

FIG. 2. Observed 1959–84 mean wind direction frequencies (%) at four local standard times: (a) 0900, (b) 1500, (c) 2100, and (d) 0300 LST. The weather stations are Ezeiza (EZE), Aeroparque (AER), Martín García (MGA), Punta Indio (PIN), and Pontón Recalada (PRE).

for resolving the small-scale details of the low-level circulation over the region.

The objective of this study is to show that the BLM (briefly described in section 2) is a useful tool for determining the low-level wind field "climatology" over coastal regions. For this purpose, a simple method is presented that calculates the wind climatological field as the ensemble result of a series of forecasts obtained by forcing the model with a limited number of local weather observations. Section 3 describes the method that calculates the wind direction and wind speed frequency distribution and its application to the La Plata River region in South America. Section 4 describes the model results along with the errors obtained when comparing the wind field distribution with the observations at five weather stations in the region during a 25-yr period. Section 5 presents the discussion of the results and the conclusions of the study.

2. BLM formulation

The BLM is a hydrostatic and incompressible model that has been developed by Berri (1987). The model equations are based on the three principles that govern the atmospheric motion: conservation of momentum, mass, and energy. Since the model is formulated for studying the atmospheric circulation in the boundary layer, the vertical component of the equation of motion becomes the hydrostatic equation and the mass conservation principle is approximated by the continuity equation for an incompressible fluid. Since the model is dry, all energy sources have been neglected, except the surface heating, so that the energy equation reduces to the conservation of potential temperature. The BLM equations are

$$\frac{\partial u}{\partial t} = -u\frac{\partial u}{\partial x} - v\frac{\partial u}{\partial y} - w\frac{\partial u}{\partial z} - \alpha_0\frac{\partial p}{\partial x} + fv + \frac{\partial}{\partial x}\left(K_{mh}\frac{\partial u}{\partial x}\right) + \frac{\partial}{\partial y}\left(K_{mh}\frac{\partial u}{\partial y}\right) + \frac{\partial}{\partial z}\left(K_{mz}\frac{\partial u}{\partial z}\right), \quad (1)$$

$$\frac{\partial v}{\partial t} = -u\frac{\partial v}{\partial x} - v\frac{\partial v}{\partial y} - w\frac{\partial v}{\partial z} - \alpha_0\frac{\partial p}{\partial y} - fu + \frac{\partial}{\partial x}\left(K_{mh}\frac{\partial v}{\partial x}\right) + \frac{\partial}{\partial y}\left(K_{mh}\frac{\partial v}{\partial y}\right) + \frac{\partial}{\partial z}\left(K_{mz}\frac{\partial v}{\partial z}\right), \quad (2)$$

TABLE 1. Mean wind speed by wind sector (m s^{-1}), at the four main observing times of the day, at the five weather stations of the study: EZE, AER, MGA, PIN, and PRE. The averaging period is 1959–84.

	N	NE	E	SE	S	SW	W	NW
0300 LST								
EZE	3.8	3.5	2.9	3.7	4.0	3.5	3.2	3.2
AER	5.2	5.2	3.9	5.1	5.7	4.7	4.2	4.3
MGA	4.1	4.6	4.5	5.3	6.1	4.8	4.3	4.3
PIN	4.6	4.6	4.7	4.8	5.0	4.6	3.9	4.4
PRE	6.4	7.0	6.5	7.1	8.3	9.0	6.8	6.1
0900 LST								
EZE	4.1	4.2	3.7	4.4	4.7	4.1	3.6	3.7
AER	4.7	4.4	3.7	5.3	5.7	5.1	4.8	4.4
MGA	4.4	4.9	4.7	5.8	6.1	4.8	4.2	4.3
PIN	5.1	5.0	5.3	5.5	5.1	4.8	4.4	5.0
PRE	6.4	6.0	5.6	7.5	7.6	7.8	7.1	6.2
1500 LST								
EZE	4.7	4.6	4.7	5.0	5.3	5.4	5.0	4.6
AER	3.9	2.9	3.5	5.3	6.6	6.7	6.6	5.7
MGA	3.7	3.9	4.2	4.7	4.2	4.4	4.3	3.5
PIN	5.4	4.5	5.6	6.0	6.0	5.9	5.7	6.2
PRE	3.9	4.8	5.5	6.4	6.7	7.0	5.8	5.4
2100 LST								
EZE	3.1	2.9	3.6	4.5	4.1	3.5	3.1	2.8
AER	3.8	3.2	4.1	5.4	5.9	5.1	4.1	3.6
MGA	3.5	4.3	4.5	5.6	5.9	5.2	4.2	3.6
PIN	3.7	4.1	4.8	4.9	5.3	4.5	3.7	3.8
PRE	4.4	5.3	6.8	7.5	7.7	8.3	6.3	5.1

$$\frac{\partial\theta}{\partial t} = -u\frac{\partial\theta}{\partial x} - v\frac{\partial\theta}{\partial y} - w\frac{\partial\theta}{\partial z} + \frac{\partial}{\partial x}\left(K_{\theta h}\frac{\partial\theta}{\partial x}\right) + \frac{\partial}{\partial y}\left(K_{\theta h}\frac{\partial\theta}{\partial y}\right) + \frac{\partial}{\partial z}\left(K_{\theta z}\frac{\partial\theta}{\partial z}\right), \tag{3}$$

$$\frac{\partial w}{\partial z} = -\frac{\partial u}{\partial x} - \frac{\partial v}{\partial y}, \tag{4}$$

$$\frac{\partial p_0}{\partial z} = -\frac{g}{\alpha_0}, \tag{5}$$

$$\frac{\partial p'}{\partial z} = \frac{g}{\alpha_0}\frac{\theta'}{\theta_0}, \tag{6}$$

$$p = p_0 + p', \quad \text{and} \tag{7}$$

$$\theta' = \theta - \theta_0. \tag{8}$$

All symbols in the equations have their usual meteorological meanings, the subscript 0 refers to a horizontal mean value over the entire domain, and the prime refers to a local departure from the horizontal mean value. Equations (1)–(3) are the forecast equations for the u and v wind components and potential temperature θ, respectively. Equations (4)–(8) are the diagnostic equations for the vertical motion w, standard pressure p_0, pressure perturbation p', total pressure p, and potential temperature perturbation θ', respectively. Equations (1)–(3) are solved from the top of the surface layer (z = 40 m) to the material top of the model by a semi-implicit numerical scheme. Within the constant flux layer, the similarity theory is applied and the forecast equations become the well-known diagnostic equations, that is, the logarithmic vertical profiles of wind and potential temperature, as a function of stability. The boundary conditions at the top of the model are $u = u_g$, $v = v_g$, and $w = p' = \theta' = 0$, where u_g and v_g are the geostrophic wind components. At the lower boundary, the conditions are $u = v = w = 0$, whereas θ is defined at every time step (see section 3a). At the lateral boundaries, all of the variables are allowed to change to provide a zero gradient across the boundaries at each time step except the pressure, since its gradient supports the geostrophic wind. The model is initialized under conditions of horizontal homogeneity for all of the variables except pressure, since its gradient supports the geostrophic wind at the initial state. Thus, Eqs. (1) and (2) become the well-known Ekman layer equations:

$$\frac{\partial u}{\partial t} = f(v - v_g) + \frac{\partial}{\partial z}\left(K_{mz}\frac{\partial u}{\partial z}\right) \quad \text{and} \tag{9}$$

$$\frac{\partial v}{\partial t} = -f(u - u_g) + \frac{\partial}{\partial z}\left(K_{mz}\frac{\partial v}{\partial z}\right), \tag{10}$$

in which the pressure force terms are replaced by the expressions of the geostrophic equilibrium with constant u_g and v_g. Equation (5) is integrated once and Eqs. (9) and (10) are integrated during three inertial periods (about 60 h at this latitude) to remove any possible inertial oscillations from the solution. Thus, the steady-state solution achieved for u and v at every grid point of the domain depends only on the particular values adopted at the upper and lower boundaries. These are defined from the 0900 LST observations and are kept constant during the initialization process. For more details about the model formulation and the numerical method of solution, please refer to Berri and Nuñez (1993).

The inner rectangle in Fig. 1 depicts the domain of the BLM forecasts that consists of 79 points in the x direction (350 km) and 58 points in the y direction (316 km). The horizontal resolution is 0.05°, which corresponds to an average of 5 km. The vertical domain has 12 levels distributed according to a log–linear spacing. The first level is the roughness length z_0 (equal to 0.001 m over water and 0.01 m over land), and the last one is the material top of the model at 2000 m. The intermediate levels are located at the following heights: 10, 40, 80, 140, 220, 350, 550, 800, 1100, and 1500 m.

3. Low-level wind climatology

The low-level climatological wind field of the model is defined as the ensemble result obtained by running a series of 18-h forecasts. Each ensemble member is a forecast obtained by forcing the model with a different upper and lower boundary condition defined from the local observations. The upper boundary condition consists of a given value of wind direction and wind speed at the top of the model, defined from the Ezeiza radiosonde observations (EZE in Fig. 2). The lower boundary condition consists of a surface heating function (see section 3a), defined from the temperature observations at the surface weather stations in the region. The ensemble result is obtained by averaging the wind direction and wind speed of all of the ensemble members. The data correspond to 1959–84, the only extended period with complete observations available in a suitable manner for this study. The model results are validated at 0300, 0900, 1500, and 2100 LST, which are the times of the day when the observations are available in the historical database. Because the model is initialized at 0900 LST, the 18-h forecast runs until 0300 LST of the following day, which is the last time of validation.

a. Boundary conditions

The model ensemble consists of 192 members, each one characterized by a wind direction and a wind speed at the top of the model. The 192 members correspond to 16 wind direction classes (N, NNE, NE, . . . , NNW), and 12 wind speed classes with the following upper bounds in meters per second: 2, 3, 4, 5, 6, 7, 8, 9, 10, 12, and 14, with the last class representing wind speeds greater than 14 m s^{-1}. Each ensemble member has a probability of occurrence p_j ($j = 1, \ldots, 192$) that is determined from the mean wind frequency distribution of the 0900 LST Ezeiza radiosonde data for the period 1959–84.

For each ensemble member, the surface heating function defines the temperature at the surface as follows: $T(x, y, t) = T_0 + F_1(t)F_2(x, y)$, where T_0 is the daily mean temperature of the ensemble, $F_1(t)$ defines the daily cycle of the maximum river–land temperature difference, and $F_2(x, y)$ defines the river–land temperature difference as a function of the distance between every (x, y) point and the coast. Except near the coasts, the horizontal air temperature gradients over the land and over the river are much smaller than the river–land air temperature gradient. Thus, the main forcing that drives the model at the surface is the daily variation of the horizontal air temperature difference across the coasts. Two weather stations are chosen for determining this forcing: one on the land (EZE) and the other in the river (PRE). The temperature difference $T_{\mathrm{EZE}} - T_{\mathrm{PRE}}$ is calculated from the four daily observations at 0300, 0900, 1500, and 2100 LST. Then, the mean value is obtained as the average of all of the days on which the Ezeiza radiosonde observation corresponds to every wind direction and wind speed class at the top of the model. Thus, for each ensemble member there are four daily temperature differences, which are interpolated by means of a harmonic analysis in order to obtain $F_1(t)$. Figure 3 depicts typical $F_1(t) = T_{\mathrm{EZE}} - T_{\mathrm{PRE}}$ curves as monthly mean values for four different months of the year. The land–river temperature difference is defined as follows: $F_2(x, y) = \{1 + \tanh[s(x, y)/B]\}/2$, where $s(x, y)$ is the minimum distance from every grid point to the coast (positive over the land and negative over the river). The hyperbolic tangent distributes the land–river temperature difference symmetrically with respect to the coasts. In this study the parameter B is set equal to 1000 m, which provides 75% (90%) of the temperature change over a distance of $2B$ ($3B$) across the coasts. Different B values were tested, and the adopted one minimized the averaged error of the wind distribution. Figure 4 shows an example of $F_2(x, y)$ as a function of the perpendicular distance to the coast, across a narrow band centered at the coastline. Over the river and away from the coast, the surface temperature $T(x, y, t) = T_0$ remains constant, since $F_2(x, y) = 0$. Over land and away from the coast, the surface temperature develops a full daily cycle given by $T(x, y, t) = T_0 + F_1(t)$, since $F_2(x, y) = 1$. At the lateral boundaries, all forecast variables, except pressure, are allowed to change to provide a zero gradient across the boundaries at each time step.

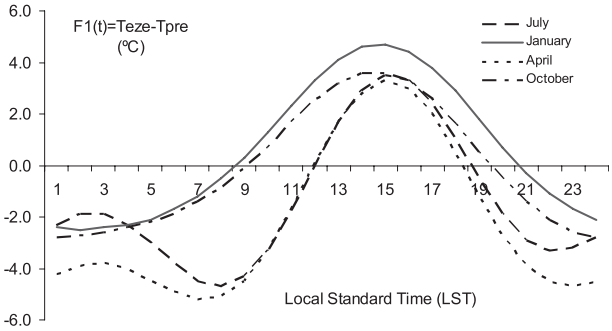

FIG. 3. Typical hourly interpolated $F_1(t)$ curves (°C) from the temperature difference TEZE minus TPRE observed at 0300, 0900, 1500, and 2100 LST. The curves shown are monthly mean values for four different months of the year.

b. Model validation

Each ensemble member provides a forecast of the horizontal wind components u and v at 10 m and contributes to the wind field climatology with a probability p_j with $j = 1, \ldots, n$ ($n = 192$). The u and v forecast is

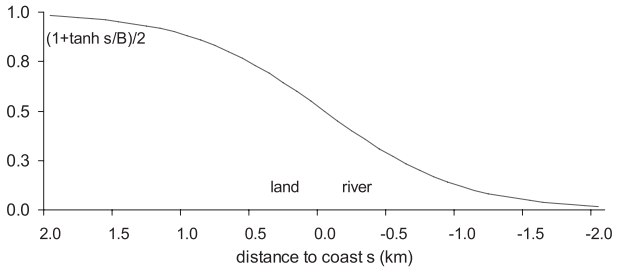

FIG. 4. Example of $F_2(x, y)$ as a function of the perpendicular distance to the coast, across a narrow band centered at the coastline, with parameter $B = 1000$ m.

expressed as a wind direction d (degrees from the north) and a wind speed $V = (u^2 + v^2)^{1/2}$ (m s^{-1}). The wind direction d defines the wind sector identified by index $i = 1$–9 [clockwise from N ($i = 1$) to NW ($i = 8$), with $i = 9$ indicating calm, i.e., wind speeds smaller than a given threshold as discussed below]. Matrices $\mathbf{D}^k_{i,j}$ and $\mathbf{V}^k_{i,j}$ store the wind direction and wind speed forecasts, respectively, in which indices $k = 1$–4 represent 0300, 0900, 1500, and 2100 LST, respectively.

Thus, the wind direction forecast simply consists of the occurrence of a given wind sector, and matrix $\mathbf{D}^k_{i,j}$ counts the number of cases. Once the jth ensemble member forecast is completed, the quantity p_j is added to the (i, j, k) component of matrix $\mathbf{D}^k_{i,j}$, and the quantity Vp_j is added to the (i, j, k) component of matrix $\mathbf{V}^k_{i,j}$. After completing the series of forecasts, the elements of matrix $\mathbf{D}^k_{i,j}$ are either zero or p_j, and $\sum_{i=1}^{9}\sum_{j=1}^{n}\mathbf{D}^k_{i,j} = 1$, since $\sum_{j=1}^{n} p_j = 1$. At every jth and kth element of matrices $\mathbf{D}^k_{i,j}$ and $\mathbf{V}^k_{i,j}$, only one of the nine ith elements is not zero, that is, the one that corresponds to the occurring wind direction sector.

At every grid point, the wind direction frequency distribution f^k_i obtained with the model (in percent) is

$$f^k_i = 100\sum_{j=1}^{n}\mathbf{D}^k_{i,j} \tag{11}$$

and the corresponding mean wind speed per wind sector v^k_i (m s^{-1}) is

$$v^k_i = \sum_{j=1}^{n}\mathbf{V}^k_{i,j}\Big/\sum_{j=1}^{n}\mathbf{D}^k_{i,j}, \tag{12}$$

since the $\mathbf{V}^k_{i,j}$ elements are of the form Vp_j and the $\mathbf{D}^k_{i,j}$ elements are of the form p_j.

The relative error in wind direction is defined as $e(d^k_i) = (f^k_i - f^k_{oi})/f^k_{oi}$, and the relative error in wind speed is defined as $e(v^k_i) = (v^k_i - v^k_{oi})/v^k_{oi}$. In these expressions, f^k_{oi} and v^k_{oi} are the mean observed wind direction frequency distribution and mean wind speed per wind sector, respectively, at the five surface weather stations of the study. The model distributions f^k_i and v^k_i are calculated with the averaged value of the four grid points that surround every weather station.

The averaged model errors are expressed as the root-mean-square value of the relative error (RMS), in wind direction Er($\mathbf{D}^k$), from Eq. (11), and wind speed Er($\mathbf{V}^k$), from Eq. (12), both weighted by the mean observed wind direction frequency f^k_{oi}, as follows:

$$\mathrm{Er}(\mathbf{D}^k) = \left\{\sum_{i=1}^{9} f^k_{oi}[e(d^k_i)]^2\Big/\sum_{i=1}^{9} f^k_{oi}\right\}^{1/2} \quad \text{and} \tag{13}$$

$$\mathrm{Er}(\mathbf{V}^k) = \left\{\sum_{i=1}^{9} f^k_{oi}[e(v^k_i)]^2\Big/\sum_{i=1}^{9} f^k_{oi}\right\}^{1/2}. \tag{14}$$

4. Model results

a. Annual mean

Figure 5 presents the wind direction frequency distribution and averaged wind speed by sector, obtained from the model according to Eqs. (11) and (12) (one in every six grid points is plotted). It represents the averaged value of the four times of the day, when the observations are available in the database for the period 1959–84. Since the model is initialized with the observations at 0900 LST, the 6-h forecast is validated at 1500 LST, the 12-h forecast is validated at 2100 LST, and the 18-h forecast is validated at 0300 LST. The 0900 LST forecast is taken after a 30-min integration to allow for the model spinup.

The weather stations report the observed wind direction in eight compass sectors, and a ninth category that corresponds to calm wind, which means that the wind speed is below the instrument threshold. For the purposes of model validation, a calm wind observation represents a problem since the model never predicts a zero wind speed. Calm wind observations over the region are variable and depend on the weather station and time of the day, and on occasion they exceed 30% of the observations. Thus, the inappropriate handling of the calm wind predictions may have a significant impact on the model errors, and therefore it was necessary to adopt a criterion to overcome this problem. Test runs were conducted with the model with the purpose of determining the wind speed value below which the resultant percentage of calm winds would match the observations at the nearby weather station. This matching value was then adopted as the wind speed threshold below which the model result would be considered to be

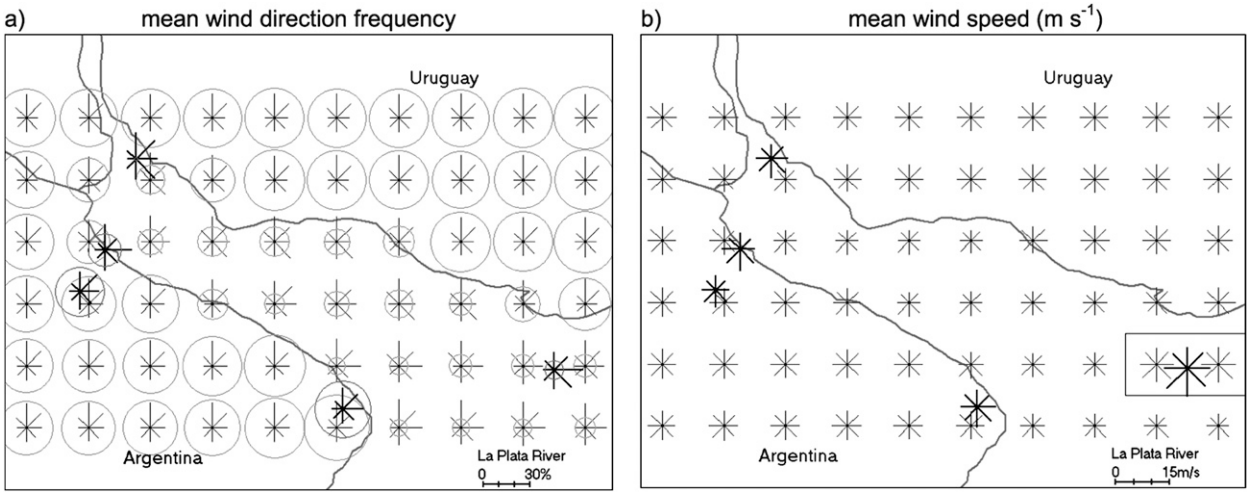

FIG. 5. (a) Mean wind direction frequency (%) and (b) mean wind speed by sector (m s^{-1}) at 10 m. Model results are plotted with thin lines, and observations of the five weather stations of the study are plotted with thick lines. Circles in (a) represent the frequency of calm wind (see the text for details). The rectangular box on the right-hand side of (b) surrounds the model grid points that are plotted at 21 m (see the text for details). The averaging period is 1959–84.

a calm wind. The thresholds varied depending on the time of the day and the position of the weather station in the domain. The nearby grid points to the weather stations over land displayed similar results, although with values that were always greater than those of the grid points that were nearby to the river weather stations. The set of wind speed thresholds adopted for the grid points over land (m s^{-1}) is 1.6, 2.6, 1.4, and 1.4 at 0300, 0900, 1500, and 2100 LST, respectively. For the grid points over the river, the wind speed thresholds (m s^{-1}) are 0.6, 0.8, 0.8, and 0.6 at 0300, 0900, 1500, and 2100 LST, respectively.

The wind sectors with higher frequencies obtained with the model are N, NE, E, SE, and S, in coincidence with the observations (Fig. 5a). However, the dominant wind sectors vary according to the position over the domain and, in general, there is more contrast between points that are closer to the coasts and over the river. Over land and far away from the river, N and NE are, in this order, the wind sectors that display the higher frequencies. Over the river, the wind direction distributions are different than over land and the E and SE wind sectors become, depending on the position, the dominant ones. The only two weather stations in the river are located at both ends, MGA at the river spring and PRE at the river mouth, and therefore it is not possible to verify the model results along the river. For example, the wind direction distribution obtained with the model over the river centerline resembles the PRE observations, that is, relatively high frequencies of the E and SE wind directions. However, the model results over the river mouth, with N and NE as the dominant wind directions, differ from the PRE observations with predominantly E and SE wind directions. This may be due to the fact that the grid points over this area are far away from the coast and have, therefore, less influence of the river–land surface thermal contrast. At the other end of the river, the wind directions obtained with the model have a better agreement with the MGA observations. Over land there are only three weather stations with available observations for this study. The wind direction distributions obtained with the model agree better with the observations at EZE and PIN than they do at AER. The first two weather stations are located a few tens of kilometers away from the coast, whereas AER is so close to it (about 500 m) that the horizontal resolution of the model may be a limiting factor.

Figure 5b shows the averaged wind speed by sector obtained with the model, as well as the observed wind speed at the five weather stations in this study. The wind instrument at PRE is at 21 m above the surface so that the model grid points within the rectangular box on the right-hand side of Fig. 5b are plotted at that height. Throughout the domain, the model wind speeds are in general slightly greater in the S, SW, and W wind sectors, in comparison with the others. The observations display a similar pattern, with the exception of PIN, which shows a smaller difference among wind sectors. There is also general agreement between the magnitude of the observed and modeled wind speeds, with the exception of the neighboring points to PRE where the observed wind speeds are clearly greater.

Figure 6 shows the percentage RMS of relative errors produced by the model in wind direction and wind speed,

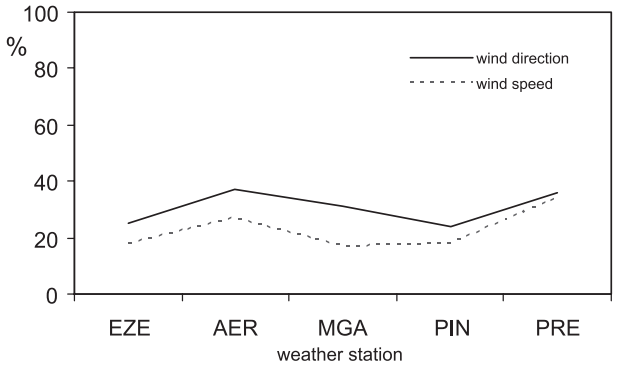

FIG. 6. Percentage RMS of the model relative errors in wind direction [Eq. (13)] and wind speed [Eq. (14)], averaged over the four grid points that surround every weather station: EZE, AER, MGA, PIN, and PRE. The averaging period is 1959–84.

according to Eqs. (13) and (14), respectively, averaged over the four grid points that surround every weather station. At the five weather stations, the error in wind speed is smaller than the error in wind direction. As discussed in the previous paragraph, the largest errors occur at PRE, whereas the smallest ones are at EZE and PIN. AER and MGA display errors with intermediate values in comparison with the other weather stations. The smallest errors are obtained at the weather stations located over land and away from the coast, because AER, which is also over land but very close to the coast, shows the second greatest error among the five weather stations. As mentioned above, the model resolution of 5 km may be the limiting factor responsible for the relatively large wind errors at AER.

The surface wind direction frequency distribution obtained with the model at four times of the day is shown in Fig. 7, together with the local observations. The regions along the river and over land near the coasts display more variability among the dominant wind sectors throughout the day. For example at 0900 LST (Fig. 7b), the dominant wind sectors are N and NE, while at 1500 LST (Fig. 7c) they are E and SE. This change is well represented by the model—in particular, the shift toward the E sector while the SE sector is more dominant over the central part of the river. Another particular aspect at the river mouth is the significant change in the dominant wind direction throughout the day, since the N and NE sectors at 0300 LST (Fig. 7a) and 0900 LST (Fig. 7b) become E, SE, and S at 1500 (Fig. 7c) and 2100 LST (Fig. 7d), which is reasonably well reproduced by the model. At the river spring, MGA shows predominance of the N and NE sectors at 0900 LST (Fig. 7b), in coincidence with the model results. At 1500 LST (Fig. 7c), MGA displays S, N, and SE as the dominant sectors, whereas the model shows the N, NE, and SE sectors around MGA, with increasing frequency of the SE and S wind sectors toward the centerline of the river. At 2100 LST (Fig. 7d), the MGA observations display the predominance of the SE, E, and NE sectors, and the model agrees in the case of the SE and NE sectors, whereas the presence of E winds becomes more evident at the centerline and toward the river mouth. Over land at 0900 LST (Fig. 7b), the dominant sectors are N and NE, in agreement with the model results. At 1500 LST (Fig. 7c) the AER observations show the highest frequency in the E sector, but the model indicates the NE sector. There is also good agreement of the model results with the observations at EZE in the N and NE wind sectors and at PIN in the N, NE, and E wind sectors. At 2100 LST (Fig. 7d) the observations show an overall predominance of the E and SE sectors, in agreement with the model results, although the latter displays a significant N frequency—in particular, toward the river mouth—that is not revealed by the observations. At 0300 LST (Fig. 7d), the observations show the N, NE, E, and SE sectors as the dominant ones, whereas the model agrees with the N and E sectors, in general, although the NE frequency is relatively small—in particular, over the river and over land near the coast.

Figure 8 shows the mean surface wind speed by sector obtained with the model, together with the observations of the five weather stations of the study at four times of day. As indicated before, the grid points that surround PRE (rectangular box on the right-hand side of each panel in Fig. 8) are plotted at 21 m above the surface in coincidence with the height of the wind instrument. In general, and throughout the domain, the observed and modeled mean wind speeds of all sectors are similar. The major observed contrast is between the wind speeds over the river and over land. For instance, at 0300 LST the wind speed over the river is clearly larger than over land, but at 1500 LST the situation is the opposite and the wind speed over land is significantly greater than over the river. At 0900 and 2100 LST the wind speed contrast between land and river is minimum. This spatial pattern and the changes that take place throughout the day are confirmed by the observations.

Another way of comparing the model results with the observations is by analyzing the coincidence of the wind direction sectors with highest frequency. Table 2 lists the first three observed and modeled wind sectors with highest frequency, in decreasing order, that together amount to 40%–60% of the observations. For example, the upper-left box (EZE at 0300 LST) displays the NE, SE, and E as the first, second, and third wind sectors with highest frequency, whereas the model indicates N, E, and NE, respectively. The modeled and observed wind sectors that match are shown in boldface in Table 2, regardless of the

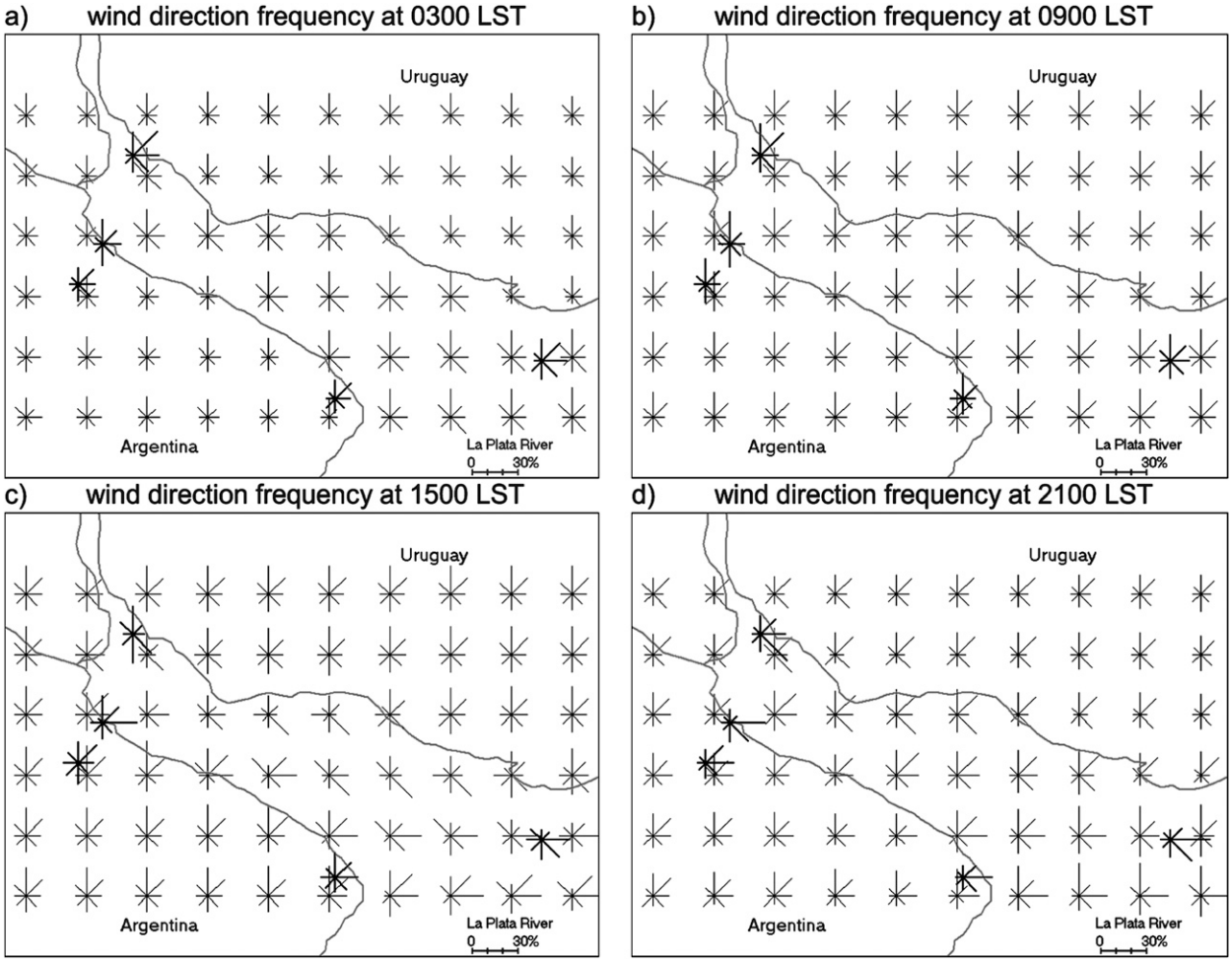

FIG. 7. Mean wind direction frequency by sector obtained with the model (thin lines) and observed at the five weather stations of the study (thick lines) at 10 m at (a) 0300, (b) 0900, (c) 1500, and (d) 2100 LST. The north wind direction points upward, and each tick mark of the scale in the lower-right corner represents a 10% frequency. The averaging period is 1959–84.

order in which they agree, since in some cases the ranking is defined by a few percent points. The best situation is when the three sectors match in the same order, as for example at 0900 LST at EZE, whereas the worst case is at 2100 LST at AER, when only the highest observed frequency is captured by the model but in third place. There is better agreement at the five points at 0900 and 1500 LST, since the average number of hits is 2.4, whereas at 0300 and 2100 LST the average number of hits is 1.6. At PRE the model shows less overall agreement with the observed predominant wind directions, as the average number of hits is 1.75. At the other four locations, the model presents similar behavior: at EZE, AER, and PIN the average number is 2.25 and at MGA it is 2.0. In particular, AER shows contrasting results because it is the only place with three hits occurring twice, that is, at 0900 and 1500 LST, whereas at 2100 LST it shows only one hit.

The model errors are not constant throughout the day, as can be seen in Fig. 9, which shows the percentage RMS of relative error, averaged over the five weather stations. Except at 0900 and 1500 LST, the wind speed error is much smaller than the wind direction error, and it shows a minor dependence on the time of the day. The error in the wind direction varies more throughout the day; it is minimum at 0900 LST and maximum at 2100 LST. The time evolution of the model errors does not follow a straightforward deterioration with time since the 13-h (2100 LST) forecast error is larger than the 19-h (0300 LST) forecast error.

Figure 10 shows the model errors in wind direction (top panel) and wind speed (bottom panel) as a function of weather station and time of day. As mentioned before, wind direction errors (Fig. 10a) are more variable with time and space than wind speed errors (Fig. 10b).

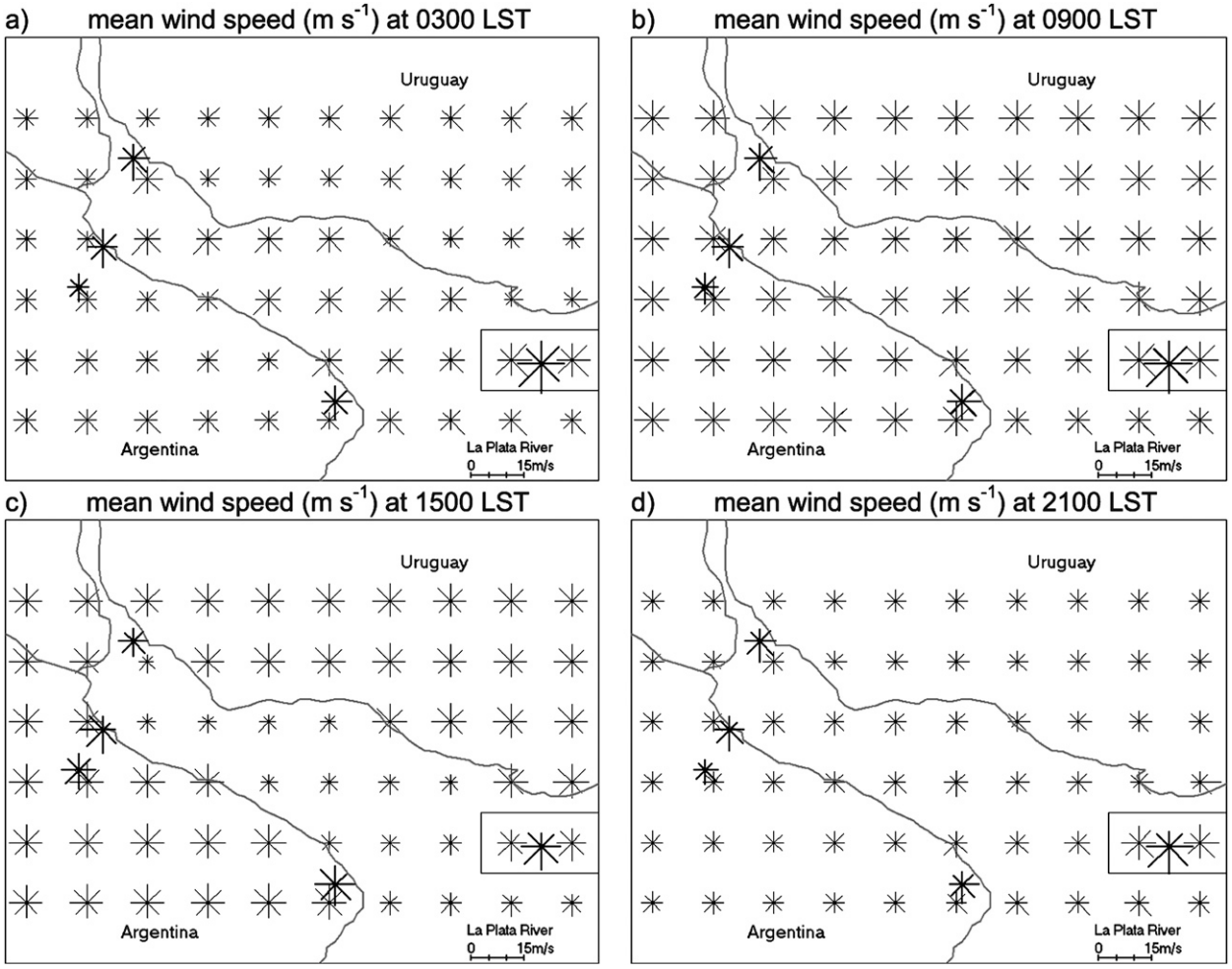

FIG. 8. Mean wind speed by sector obtained with the model (thin lines) and observed at the five weather stations of the study (thick lines) at 10 m at (a) 0300, (b) 0900, (c) 1500, and (d) 2100 LST. The rectangular box on the right-hand side of each panel surrounds the model grid points that are plotted at 21 m (see the text for details). Each tick mark of the scale in the lower-right corner represents 5 m s^{-1}. The averaging period is 1959–84.

At 0900 and 1500 LST, wind direction errors are minima and very small everywhere, whereas at 0300 and 2100 LST they are generally at their maxima—in particular, at AER and PRE. At MGA the wind direction error shows a small variation throughout the day. On the other hand, PRE, which has the greatest combined error in wind direction and wind speed (see Fig. 6) and displays strong daily variations, presents the minimum wind direction error at 0900 LST. The wind speed errors (Fig. 10b) are more homogeneous throughout the domain and present a similar variation with time of the day at the five weather stations.

b. Seasonal mean

To assess the seasonal performance of the model, the same method as described in section 3a is applied to the four seasons of the year defined as follows: summer is December–February, autumn is March–April, winter is June–July, and spring is September–November. Figure 11 shows the model errors at the five weather stations as a function of the season of the year for wind direction (top panel) and wind speed (bottom panel). In the case of wind direction (Fig. 11a), the model error is minimum in winter and maximum in summer at the five locations. In spring the model errors are smaller that in autumn, and the annual error is very similar to that of winter. The only exception is PRE, where the autumn wind direction error is smaller than the annual one. The spread of the wind direction errors among the different seasons is similar at the five weather stations. The wind speed errors (Fig. 11b) display no seasonality, except to a minor degree in the case of EZE, which has the minimum in summer and the maximum in winter and autumn, in contrast with the case of the wind direction error.

TABLE 2. First three observed and modeled wind sectors with highest frequency, in decreasing order, at the five weather stations of the study as a function of time of day. The matching wind direction sectors, regardless of their order, are shown in boldface.

		0300 LST			0900 LST			1500 LST			2100 LST		
EZE	Model	N	**E**	**NE**	**N**	**NE**	**S**	**N**	**NE**	E	**NE**	**E**	N
	Obs	**NE**	SE	**E**	**N**	**NE**	**S**	**NE**	**N**	S	**E**	**NE**	SE
AER	Model	**N**	E	**NE**	**N**	**NE**	**S**	**N**	**NE**	**E**	N	NE	**E**
	Obs	**N**	S	**NE**	**N**	**S**	**NE**	**E**	**N**	**NE**	**E**	SE	S
MGA	Model	**N**	NW	**NE**	**N**	**NE**	S	**N**	NE	**SE**	N	**NE**	**SE**
	Obs	**NE**	E	**N**	**NE**	**N**	SE	S	**N**	**SE**	**SE**	E	**NE**
PIN	Model	**N**	**E**	NW	**N**	**NE**	S	**N**	**NE**	**E**	**NE**	N	**E**
	Obs	NE	**N**	**E**	**N**	**NE**	SW	**N**	**E**	**NE**	**E**	SE	**NE**
PRE	Model	**N**	**E**	SE	**N**	**NE**	S	**E**	NE	**S**	N	NE	**S**
	Obs	NE	**E**	**N**	**N**	**NE**	E	**E**	SE	**S**	E	SE	**S**

5. Discussion and conclusions

A mesoscale boundary layer model is used for simulating the high-horizontal-resolution low-level wind field climatology for the La Plata River region of South America. A simple method is developed with the purpose of calculating the climatological surface wind field with the ensemble of a series of daily forecasts obtained by forcing the model with limited local weather observations. The BLM is a primitive equation, dry, hydrostatic, and incompressible model that has been employed in different studies in the region (Berri and Nuñez, 1993; Sraibman and Berri 2009). The horizontal model domain has 79×58 points (350 km $\times$ 316 km), with a horizontal resolution of 0.05° (5-km average). The BLM upper boundary condition consists of a given value of wind direction and wind speed taken from the only local radiosonde observation. The lower boundary condition is a surface heating function that defines the daily cycle of the land–river temperature contrast from the temperature observations of the surface weather stations in the region. The ensemble results are used for calculating the surface mean wind direction frequency distribution and mean wind speed by wind direction sector. The ensemble consists of 192 members, and each member produces a daily forecast. The ensemble average defines the mean wind frequency distribution in which each member participates with a probability calculated with the observations. The BLM results are validated with the 0300, 0900, 1500, and 2100 LST 1959–84 surface wind observations at five weather stations in the region (two over the river and three over land). Since the model is initialized at 0900 LST, the 18-h forecast runs until 0300 LST of the following day, which is the last time of validation. The averaged model errors are expressed as the RMS of the relative errors (in percent) in the wind direction frequency distribution and the mean wind speed by wind sector, both weighted by the mean observed wind direction frequency.

The wind observations over the region display a significant daily cycle since the predominant wind direction sectors change more than one quadrant, as a result of the daily cycle of the land–river surface thermal contrast. The annual mean wind direction frequency distribution and mean wind speed by sector obtained with the model represent very well the observations. The averaged RMS error is 31% for wind direction and 23% for wind speed. The wind direction sectors with higher frequencies obtained with the model are N, NE, E, SE, and S, in agreement with the observations. The dominant wind direction sector varies throughout the day depending on the position over the domain and, in general, grid points nearby to the coast and over the river show more daily contrast. The predominant wind direction obtained with the model shifts between the morning and the afternoon from N to E over land and from N to SE over the river. This result agrees with the observations, with the exception of the grid points over the river mouth where the model is unable to reproduce the observed wind shift to the SE in the afternoon. In general, model results are better around the river spring than the river mouth, probably because of a major influence of the river–land surface thermal contrast over the region where the river is narrower. The mean wind speeds obtained with the

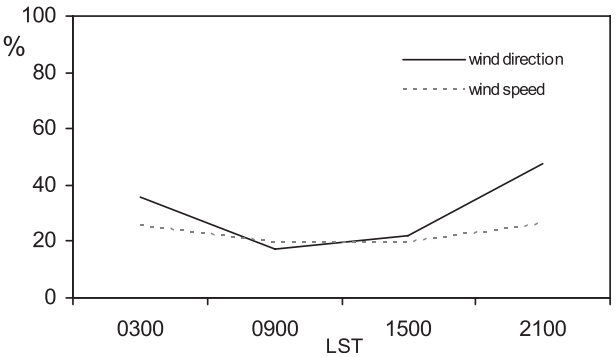

FIG. 9. Percentage RMS of the model relative errors in wind direction [Eq. (13)] and wind speed [Eq. (14)], as a function of the local standard time, averaged for the five weather stations. The averaging period is 1959–84.

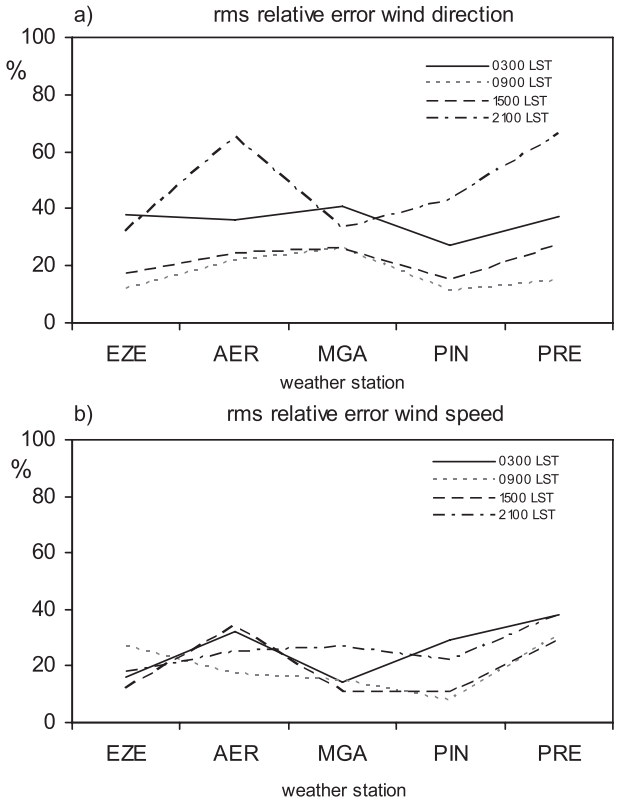

FIG. 10. Percentage RMS of the model relative errors as a function of the time of day, in (a) wind direction [Eq. (13)] and (b) wind speed [Eq. (14)], averaged over the four grid points that surround every weather station: EZE, AER, MGA, PIN, and PRE. The averaging period is 1959–84.

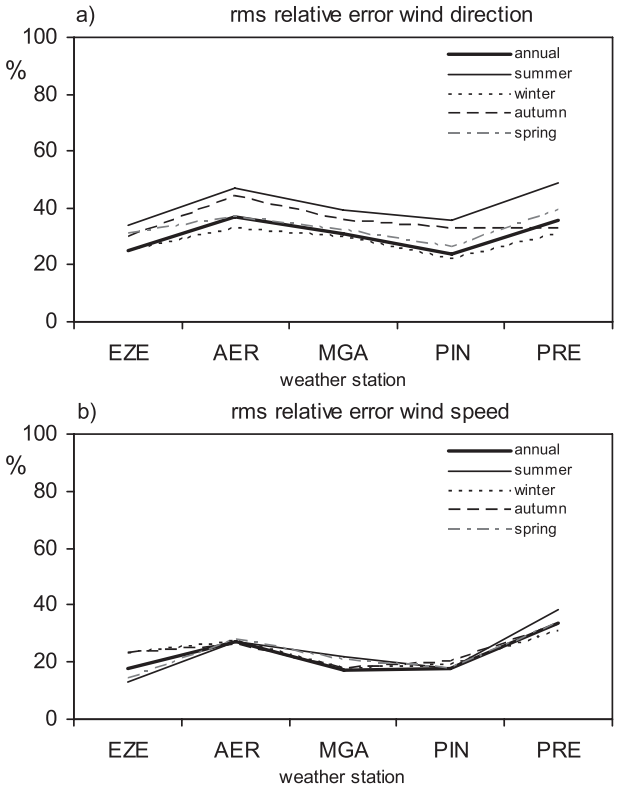

FIG. 11. Percentage RMS of the model relative errors as a function of season of the year, in (a) wind direction [Eq. (13)] and (b) wind speed [Eq. (14)]. Values are the average of the four grid points that surround every weather station: EZE, AER, MGA, PIN, and PRE. The averaging period is 1959–84.

model are slightly greater from the S, SW, and W sectors, in good agreement with the observations. In addition, the model represents very well the difference in the wind speed magnitudes throughout the region; that is, during the daytime (nighttime) hours, the wind speeds over land are greater (smaller) than over the river.

The mean RMS error in wind speed is smaller than in wind direction around the five weather stations (23% wind speed; 31% wind direction). The wind direction errors show a strong variation with time of the day, whereas wind speed errors are almost constant. The RMS errors are smaller at 0900 LST (17% wind direction; 20% wind speed) and at 1500 LST (22% wind direction; 19% wind speed) and are greater at 2100 LST (48% wind direction; 26% wind speed). The model is initialized at 0900 LST, and the forecast does not show a systematic deterioration with time, since the 13-h (2100 LST) forecast error (48% wind direction; 26% wind speed) is larger than the 19-h (0300 LST) forecast error (36% wind direction; 26% wind speed). The grid points nearby to the weather stations located some tens of kilometers inland (i.e., around EZE and PIN) display smaller errors than those that are closer to the coast (i.e., around AER), suggesting that nearby to the coastal areas the horizontal model resolution may be a limiting factor. The seasonal climatology shows the minimum wind direction error in winter and the maximum in summer, with the annual wind direction error being very similar to the winter minimum error, at the five weather stations. The spread of the wind direction errors among the different seasons of the year is similar at the five weather stations, whereas the wind speed errors reveal no seasonality. The conclusion of the study is that the BLM and the proposed ensemble mean method are useful tools for synthesizing high-resolution low-level climatological wind fields over regions with a strong diurnal cycle of surface thermal contrasts and a limited number of available weather stations.

Acknowledgments. This research was partially supported by research grants PIP5575 from Consejo Nacional de Investigaciones Científicas y Técnicas (CONICET) of Argentina, UBACYT X835 from Universidad de Buenos Aires, and PICT2005–38193 from Agencia Nacional de Promoción Científica y Tecnológica of Argentina. Also

acknowledged is the National Meteorological Service of Argentina for providing the weather station data. Special thanks are given to Jose Ares from the National Meteorological Service of Argentina for preparing the database.

REFERENCES

Berri, G. J., 1987: Thermo-hydrodynamic study of the atmospheric boundary layer over the La Plata River region with a numerical simulation model. Ph.D. thesis, University of Buenos Aires, 189 pp.

——, and M. N. Nuñez, 1993: Transformed shoreline-following horizontal coordinates in a mesoscale model: A sea–land-breeze case study. *J. Appl. Meteor.,* **32,** 918–928.

Case, J. L., J. Manobianco, J. E. Lane, C. D. Immer, and F. J. Merceret, 2004: An objective technique for verifying sea breezes in high-resolution numerical weather prediction models. *Wea. Forecasting,* **19,** 690–705.

Colby, F. P., Jr., 2004: Simulation of the New England sea breeze: The effect of grid spacing. *Wea. Forecasting,* **19,** 277–285.

Pielke, R. A., and Coauthors, 1992: A comprehensive meteorological modeling system—RAMS. *Meteor. Atmos. Phys.,* **49,** 69–91.

Simionato, C. G., C. S. Vera, and F. Siegismund, 2005: Surface wind variability on seasonal and interannual scales over Río de La Plata area. *J. Coastal Res.,* **21,** 770–783.

Sraibman, L., and G. J. Berri, 2009: Low level wind forecast over La Plata River region with a mesoscale boundary layer model forced by regional operational forecasts. *Bound.-Layer Meteor.,* **130,** 407–422.